Microstructure design of lead-free piezoelectric ceramics

S.-B. Lee [a], T.S. Key [a], Z. Liang [a], R.E. García [a,*], S. Wang [b], X. Tricoche [c], G.S. Rohrer [b],
Y. Saito [e], C. Ito [e], T. Tani [d,e,f]

[a] *School of Materials Engineering, Purdue University, West Lafayette, IN 47907-2044, United States*
[b] *Department of Materials Science and Engineering, Carnegie Mellon University, Pittsburgh, PA 15213-3890, United States*
[c] *Department of Computer Science, Purdue University, West Lafayette, IN 47907-2044, United States*
[d] *Toyota Research Institute of North America, Ann Arbor, MI 48105, United States*
[e] *Toyota Central Research & Development Laboratories, Inc., Nagatuke, Aichi 480-1190, Japan*
[f] *Toyota Technological Institute, Nagoya 468-8511, Japan*

Abstract

Computational and experimental methodologies are integrated into a novel combined technique to define microstructure design criteria and maximize the properties of rhombohedral $Bi_{0.5}Na_{0.4}K_{0.1}TiO_3$, from untextured (1 MRD), $d_{33} = 155$ pC/N, to textured (4.41 MRDs), $d_{33} = 227$ pC/N. Two-dimensional orientation maps obtained using electron backscatter diffraction on sequential parallel layers are used to computationally reconstruct three-dimensional samples, simulate the local piezoelectric grain interactions, and thus demonstrate that superior lead-free piezoelectric microstructures can be fabricated by engineering its associated crystallographic and polarization texture. Computer-generated material representations, based on the experimentally determined microstructures, were used to simulate the crystallographic orientation of each grain, as function a macroscopic polarization and crystallographic texture. Computer-generated material representations, based on the experimentally determined microstructures, were used to simulate the crystallographic orientation of each grain, as function a macroscopic polarization and crystallographic texture. The method takes advantage of the anisotropy of the properties of the underlying single-crystal phases and delivers a guide to search for material anisotropy |microstructure parameters that are optimal in piezoelectric performance and reliability, and thus establish practical links between structure and macroscopic length scales.
© 2012 Elsevier Ltd. All rights reserved.

Keywords: Microstructure reconstruction; Piezoelectric design; Crystallographic texture; Lead-free piezoelectrics

1. Introduction

Recent advances in performance of lead-free piezoelectric ceramics have demonstrated that materials near the morphotropic phase boundary can replace the equivalent lead-containing chemistries.[1–3] Lead-free reports have emerged for applications that range from actuators,[4] to force and displacement sensors and even energy harvesting devices.[5] In this context, the statistically favored crystallographic orientation alignment of the ferroelectric domains in each grain has the potential to maximize the macroscopic d_{33} response,[4] when the phases that constitute the material are assembled in polycrystalline form. Indeed, crystallographic texture engineering has demonstrated that by starting from plate-like precursor particles, through techniques such as templated grain growth (TGG) and reactive-templated grain growth (RTGG),[6–9] the macroscopic polycrystalline piezoelectric constants can be tuned. In particular, $Bi_{0.5}Na_{0.5-x}K_xTiO_3$, BNKT, has recently shown improvement in responses in the 58–168 pC/N range.[10,2,4] While the improved response compares reasonably well with PZTs at the targeted operation temperatures, the equivalent single-crystal d_{33} values promise responses on the order of 300 pC/N,[11,12] suggesting further room for improvement.

Historically, the effect of microstructure has been theoretically investigated by spatially averaging the effects of crystallographic orientation and treating the complex polycrystalline network as a homogeneous system.[13,14] Such an approach

---

* Corresponding author. Tel.: +1 765 494 0148.
 E-mail address: redwing@purdue.edu (R.E. García).

Glossary of symbols

A_{22}	normalized rhombohedral crystallographic anisotropy
A_{33}	normalized tetragonal crystallographic anisotropy
C^E_{ijkl}	stiffness tensor at constant electric field
$\vec{D}$	total polarization or displacement vector
D_i	ith component of displacement vector
E_i	ith component of electric field
d_{ijk}	piezoelectric tensor (d-form)
f	March–Dollase orientation distribution function
L	Lotgering factor
MRD	crystallographic multiples of random distribution
MRD_f	ferroelastic multiples of random distribution
MRD_F	ferroelectric multiples of random distribution
MRD_p	polarization multiples of random distribution
p	volume fraction of textured grains
p_r	volume fraction of untextured grains
r	March–Dollase texture fitting parameter
$\epsilon^{\varepsilon^T}_{ij}$	dielectric permittivity at constant total strain
ε^T_{ij}	ijth component of total strain tensor
$\overset{\leftrightarrow}{\sigma}$	stress tensor
σ_{ij}	ijth component of stress tensor

is based on deriving analytic solutions to the electromechanical fields around a piezoelectric ellipsoidal inclusion,[15,16] and has made it possible to specify the average piezoelectric behavior, particularly for perfectly poled, untextured materials.[17–21] Most recently, theoretical analyses have focused on the prediction of the equilibrium properties and domain switching behavior by starting from first principles,[22–25] or by using Taylor series expansions of the free energy of the system to define phase field or other generic energy-minimizing frameworks. These approaches effectively predict the appearance and thermodynamic stability of different types of ferroelectric domains for single-crystals,[26,27] and most recently in untextured polycrystals.[28,29] In spite of the unprecedented progress, none of the existing approaches explicitly incorporate the randomness and richness of microstructural details that a processing operation generates. Moreover, previous work rarely make direct comparisons to experimental measurements and often fail to provide guidelines on the microstructure design process. Furthermore, no practical simple engineering criteria exists to sort out what material anisotropies are amenable to be produced in polycrystalline form, and what texture (crystallographic, ferroelastic, or ferroelectric) should be induced, or if it can be physically realized.

In the present paper we demonstrate a novel methodology that integrates experimental and modeling techniques into a description that starts from measured orientation maps to reconstruct, simulate, and engineer an optimal macroscopic d_{33} response for textured polycrystalline rhombohedral BNKT. The approach incorporates the spatial distribution of the properties of the

analyzed microstructures and specifies a comprehensive description that treats all known interactions to the level of spatial resolution. Fundamental principles directly linking the single-crystal material anisotropy to the ideal microstructure are defined to provide research guidelines to access experimentally feasible chemistries, textures and poling conditions and thus realize optimal responses that will accelerate the material design cycle.

2. Theoretical framework

The electromechanical response of a volume element of material is described through the mechanical equilibrium equation and Coulomb's law in its differential form:

$$
\begin{aligned}
\nabla \cdot \overset{\leftrightarrow}{\sigma} &= \vec{0} \\
\nabla \cdot \vec{D} &= 0
\end{aligned}
\tag{1}
$$

subjected to the constitutive relations:

$$
\begin{aligned}
\sigma_{ij} &= C^E_{ijkl}\varepsilon^T_{kl} - C^E_{ijkl}d_{mkl}E_m \\
D_i &= \epsilon^{\varepsilon^T}_{ij}E_j + d_{ijk}C^E_{jklm}\varepsilon^T_{lm}
\end{aligned}
\tag{2}
$$

Each symbol and coefficient follows Nye's notation,[30] and summarized above.

The full effect of texture and the details of the correlations between neighboring grains on the macroscopic properties of rhombohedral BNKT were incorporated by three-dimensionally reconstructing experimentally measured microstructure cross-section data, as described in Section 3.

For those crystallographic textures that are experimentally inaccessible, computer-generated microstructure representations of textured polycrystals were approximated by using a numerical implementation of a Monte Carlo algorithm of a single phase isotropic grain growth system.[31] Crystallographic fiber texture was introduced by using the March–Dollase orientation probability distribution,[32] as a function of a fitting parameter r, and α, the angle made between the a-axis and the fiber axis (a cone-angle) as used by several authors[28,33,34]:

$$
p = \frac{1}{(r^2\cos^2\alpha + (1/r)\sin^2\alpha)^{3/2}}
\tag{3}
$$

For $\alpha = 0°$, p corresponds to the probability of finding a crystallographic orientation aligned parallel to a laboratory reference system direction, with respect to the probability of finding the same orientation in an untextured (perfectly random) polycrystal, *i.e.*, the Multiples of Random Distribution, MRDs, of the sample. Thus, $\text{MRD} = 1/r^3$ for a fiber-textured system.[33] Eq. (3) was included into the numerical description by using the Monte Carlo method.

The MRD representation can be directly related to well-known and widely used descriptions of crystallographic texture,
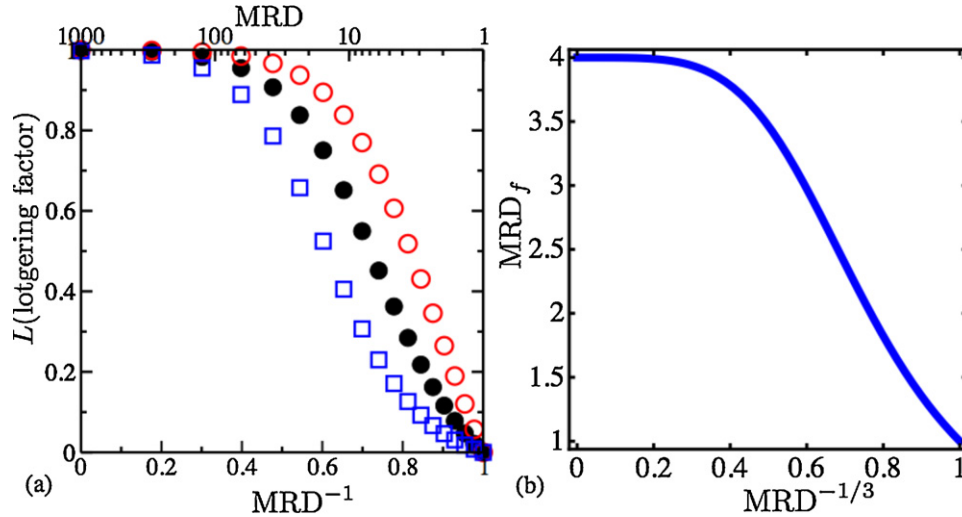
Fig. 1. (a) Lotgering factor as a function of crystallographic Multiples of Random Distribution, MRD, for a fiber-textured BNKT polycrystal. □ correspond to a $\{1\,1\,1\}$ textured material, ● to an $\{1\,0\,0\}$ textured polycrystal, and ○ to a $\{1\,1\,0\}$ textured system. Here, $p_r^{\mathcal{L}}(0\,0\,1) = 0.1787$, $p_r^{\mathcal{L}}(1\,1\,0) = 0.6299$, and $p_r^{\mathcal{L}}(1\,1\,1) = 0.0839$, based on the well-known relation $L = (p^{\mathcal{L}} - p_R^{\mathcal{L}})/(1 - p_R^{\mathcal{L}})$, where $p^{\mathcal{L}} = (\sum I_{\{h_\circ k_\circ l_\circ\}})/(\sum I_{\{h_i k_i l_i\}})$ as reported by Lotgering,[35] and using Eq. (14) (see Appendix B). (b) Ferroelastic Multiples of Random Distribution, MRD_f, as a function of crystallographic, fiber texture, MRD, for rhombohedral polycrystalline ferroelectrics. The presented set of equations relate crystallographic-based representations of texture to ferroelectric based representations of texture, as currently used by several groups in the scientific community.

such as the Lotgering factor, as summarized in Fig. 1(a) for rhombohedral BNKT,[35] or ferroelastic texture, MRD_f, as defined by Bowman et al.[36,37] MRD_f and MRD are related herein through the expression[38]:

$$MRD_f = \frac{4}{1 + \frac{81}{(1+8\times MRD)^{3/2}}} \qquad (4)$$

for the case of fiber texture. The description is graphically summarized in Fig. 1(b), and derived in Appendix B.

In addition, for a volume fraction of material, the degree of polarization, p_F, is defined as the normalized macroscopic remnant polarization of a solid aligned with the poling axis. Thus if $p_F = 0$, 50% of the ferroelectric domains have a positive and negative projection with the poling axis, the material is depoled and shows a zero macroscopic remnant polarization. And if $p_F = 1$ the average remnant polarization of all the volume elements of material has a positive projection with the poling axis, i.e., the material is perfectly poled. In terms of Multiples of Random Distribution, $MRD_p = 1 + p_F$, specifies the probability of finding a ferroelectric variant with a crystallographic axis parallel with the fiber axis of the sample. Thus, for an unpoled sample, $p_F = 0$ corresponds to $MRD_p = 1$, and for a perfectly poled sample, $p_F = 1$, corresponds to $MRD_p = 2$, i.e., it is twice as likely to sample a poled volume element of material.

Finally, ferroelectric texture is defined herein as[38]:

$$MRD_F = MRD_f \times MRD_p \qquad (5)$$

and establishes correlations between the correlated spatial distribution of domains in a polycrystal with the underlying crystallographic texture and the poling of a sample, all of them measurable quantities.
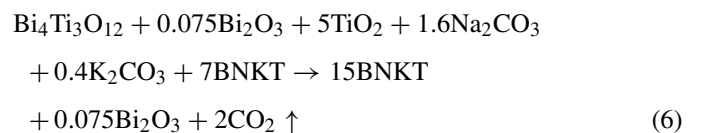
Fig. 1 allows to compare the results of the present work in terms of quantities that are directly related to processing of rhombohedral BNKT samples, and thus specify texture–property relationships in terms of four of the most widely used experimental measures of texture representations, as currently used by the ferroelectrics community.[1,6,8,7,36]

3. Experimental

Sample fabrication. Untextured BNKT ceramics were prepared by conventional powder processing. Stoichiometric amounts of Bi_2O_3 (99.99%; Kojundo Chemical Laboratory Co., Ltd.), TiO_2 (>99.7%, Ishihara Sangyo Kaisha, Ltd.), Na_2CO_3 >99.5%; Wako Pure Chemical Industries, Ltd.) and K_2CO_3 (>99.5%; Wako Pure Chemical Industries, Ltd.) were wet-mixed and heat-treated at $800\,^{\circ}C$ for 5 h to synthesize perovskite-type equiaxed BNKT powders. These powders were die-pressed at 196 MPa and sintered in O_2 at $1200\,^{\circ}C$ for 1 h.

Textured BNKT ceramics were prepared by the reactive-templated grain growth (RTGG) method as described by Tani et al.[7] Plate-like $Bi_4Ti_3O_{12}$ (BiT) particles were prepared by molten salt synthesis in NaCl-KCl flux at $1050\,^{\circ}C$ for 1 h and used as reactive templates. The plate-like BiT was mixed with Bi_2O_3, TiO_2, Na_2CO_3, K_2CO_3 and equiaxed BNKT powders in the following formula ratio in ethanol–toluene based slurry with organic binder and plasticizer, i.e.,

$$Bi_4Ti_3O_{12} + 0.075Bi_2O_3 + 5TiO_2 + 1.6Na_2CO_3$$
$$+ 0.4K_2CO_3 + 7BNKT \rightarrow 15BNKT$$
$$+ 0.075Bi_2O_3 + 2CO_2 \uparrow \qquad (6)$$

An excess Bi_2O_3 (+2%) was added to account for volatility during processing, enabling a chemistry closer to stoichiometric to be synthesized.

The slurry was tape-cast and the tape was stacked at 80 °C and a uniaxial pressure of 9.8 MPa for 10 min to form a ~2 mm thick plate. The plate was heat-treated at 600 °C for 1 h to remove organic substances before cold-isostatic pressing (CIPing) treatment at 294 MPa. The CIPed specimen was sintered at 1200 °C for 6 h in an O_2 atmosphere. The produced samples were electrically poled at 3–5 kV at 100 °C and cooled to room temperature while maintaining the applied electric field.

Piezoelectric constant measurements. To measure the longitudinal direct piezoelectric constant ($D_3 = d_{33}\sigma_{33}$, where 3 denotes the poling axis), a Pennebaker Model 8000 Piezo d_{33} Tester was employed.[46] The tester was calibrated to a known sample value of $d_{33} = 97$ pC/N.[47] The converse effect piezoelectric constant measurement ($\varepsilon_{33} = d_{33}E_3$), was determined through a Radiant Technologies Precision Workstation in conjunction with a Radiant Technologies High Voltage Interface (HVI). A Trek 5/80 High Voltage Amplifier (HVA) was used to apply an electrostatic potential of ±500 V, substantially less than the coercive voltage of the 1-1.5 mm thick samples. A bipolar triangular wave with a frequency of 1 Hz and 0.1 Hz was applied. The mechanical displacement was measured through a MTI 2100. The piezoelectric constant was extracted from the slope of the sample displacement as a function of applied electric field.

Crystal structure and texture characterization. A Bruker General Area Detector Diffraction System (GADDS) comprised of a collimated Cu Kα source, a three circle goniometer, and a two position chi stage was used. The measurements were made at a detector distance of 6 cm, $2\theta = 40°$, $\omega = 20°$ and chi = 0° and 35.26° for a total time of 600 s. 2θ vs intensity data were collected every 5° between 0° and 55° chi by integrating across chi (±2.5°) as a function of 2θ. Fiber symmetry was imposed on the sample when rotated about phi. Structure and texture measurements were refined by using the Rietveld refinement program MAUD.[48] Phase models were based on the structures reported by Jones et al.[49] Texture was fitted to an 8th order spherical harmonic function where pole figures and inverse pole figures were generated in MRD units.

Samples sectioning and reconstruction. BNKT samples were polished to have two perpendicular faces, one for analysis and the other one to provide a square edge for consistent ion-milling. The samples are attached to a 45° pre-tilted stub using conductive carbon paint and sputter-coated with ~2 nm of platinum to reduce charging. On the 45° pre-tilted stub, the sample was tilted 7° toward the ion-beam in the FIB (Nova 600, FEI company, Hillsboro, Or), or rotated 180° and tilted 25° towards the EBSD detector for data collection (EDAX, Mahwah, NJ). Circular fiducial markers were milled into the samples during the automated data collection, and were used to align the area of interest. The sample was ion-milled at 30 kV and 7 nA using a Ga+ ion beam. EBSD data were acquired using a 30 kV beam at a current of 9.5 nA. The slice thickness between subsequent serial sections was 100 nm, the in-plane resolution of the EBSD scans was 70 nm and an area approximately 20 microns by 20 microns was scanned. The EBSD patterns were indexed at a rate of approximately 35 per second, with the detector pixels binned

in 4×4 groups. The time for each 2D orientation map was 40 min and the time for each milling step was about 10 min. For the untextured sample, fifty-one serial sections were collected. For the textured sample, twenty-seven serial sections were collected, each section 400 nm apart. The normal of the sectioned plane was parallel to the fiber axis. In both cases, the orientations were indexed under the assumption of cubic symmetry. Grains were defined as groups of 100 or more voxels that were misoriented by less than 5°.

Microstructures were then reconstructed in the computer by linearly interpolating between adjacent EBSD layers. Effects such as drift and charging were subtracted from the image by using algorithms developed by Lee et al.[50] The effect of polarization direction and ferroelastic distortion direction, lost through EBSD sampling, was reintroduced by implementing a Monte Carlo algorithm, as discussed in the narrative. A value of $MRD_p = 1.8$ was used.

4. Numerical implementation

Eqs. (1) and (2) were numerically implemented through the application of the finite element method. The procedure consists on discretizing the spatial domain into subdomain collocation brick elements of homogeneous properties. The crystallographic orientation dependent electromechanical response at every volume element is specified by using: (1) the position dependent Euler angles of the reconstructed experimental microstructures, or (2) the list of crystallographic orientations that the Monte Carlo implementation of Eq. (3) generates. Computer generated microstructures were comprised of 588 grains, as described in Section 2.

For calculations based on experimentally determined orientation data, statistically representative poling values that the material can reach, MRD_p, are explored by Monte Carlo sampling the poling axis. Computer-generated microstructures also capture the effect of texture by first generating a crystallographic orientation population for the *c*-axis for a specified value of MRD that satisfies Eq. (3). For each cone-angle, α, the remaining axes of the rotated reference frame are selected by defining a direction perpendicular to the *c*-axis. The cross product of the first two directions determines the orientation of the remain axis. The two remaining (antiparallel) possibilities are defined by specifying the degree of polarization. The statistical distribution of macroscopic responses are obtained from repeated simulations for iterated Monte Carlo samples of fixed microstructural parameters. The implemented numerics generated meshes on the order of 1,350,000 elements that took on the order of 4 h of CPU time to converge to a relative tolerance of 1×10^{-6}, through the application of a GMRES solver and a multilevel preconditioner. The predicted position-dependent electromechanical fields were used to compute the volume element weighted average strain and determine the macroscopic, piezoelectric constant, d_{33}.

The methodology developed herein assumes that each grain is formed of a chemically homogeneous ferroelectric domain whose local state of polarization is fixed. In addition, no field-induced phase transitions, electric field, stress-induced
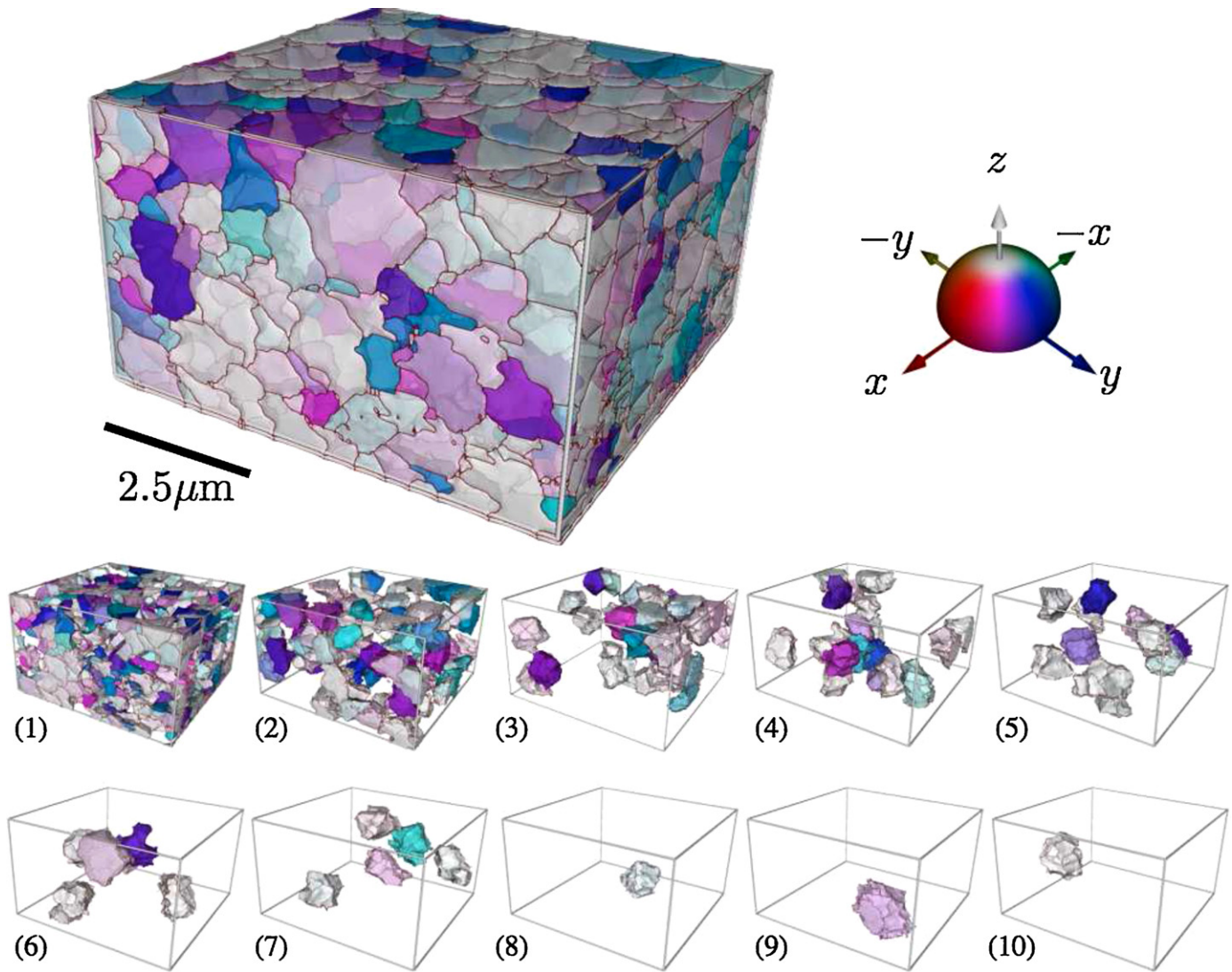
Fig. 2. Three-dimensionally reconstructed, untextured $Bi_{0.5}Na_{0.4}K_{0.1}TiO_3$. Top inset shows overall microstructure. Insets (1)–(10) bin grains into sizes of steps of 10% the entire grain size range. The average grain size is 0.89 μm, the smallest size is 0.45 μm, and the largest grain size is 9 μm. The color of each grain denotes the direction of the pseudocubic a-axis. The analysis demonstrates that untextured samples are comprised of a majority of morphologically isotropic grains. Medium and large crystals are held together by small grains.

or any extrinsic contribution to the macroscopic piezoelectric response, including domain wall contributions are included in the present simulation. Grain boundaries are assumed infinitely sharp, compared to the three-dimensional grain size; therefore, grain boundary dielectric, mechanical, and piezoelectric properties are not included in the present model. Pores, cracks, as well as point and line defects are not included in the present description, but can be easily included. Similarly, spatial ionic charges are not included in the present model. Finally, thermal or processing stresses, as well as built-in electric fields are not included, but can be easily integrated in the present theoretical framework. Physical properties of the analyzed materials are summarized in Appendix A. In particular, single-crystal rhombohedral $Bi_{0.5}Na_{0.4}K_{0.1}TiO_3$, correspond to available experimental data as reported by several authors.[12,54,11] Missing information was complemented by using numbers from rhombohedral PMN–33% PT,[53] and assuming materials share

similar normalized degree of crystallographic anisotropy, as described in Eq. (7).

5. Results and discussion

To rationalize the effect of microstructure in crystallographically textured BNKT piezoelectric ceramics, untextured and highly pseudocubic-{100}-textured $Bi_{0.5}Na_{0.4}K_{0.1}TiO_3$ samples were fabricated, macroscopically characterized, sectioned, and reconstructed in the computer as described in the Section 3. Upon poling both samples, a rhombohedral crystal structure, space group $R3c$, was identified, based on previous work, as reported by Jones and Thomas,[40] and fitted by using MAUD.[48] In particular, for the *untextured* sample, texture measurements verified a Lotgering factor of $L = 0$, or 1 MRD of crystallographic texture. Similarly, for the *textured* sample a Lotgering factor of $L = 0.5$, or 4.41 MRDs, were
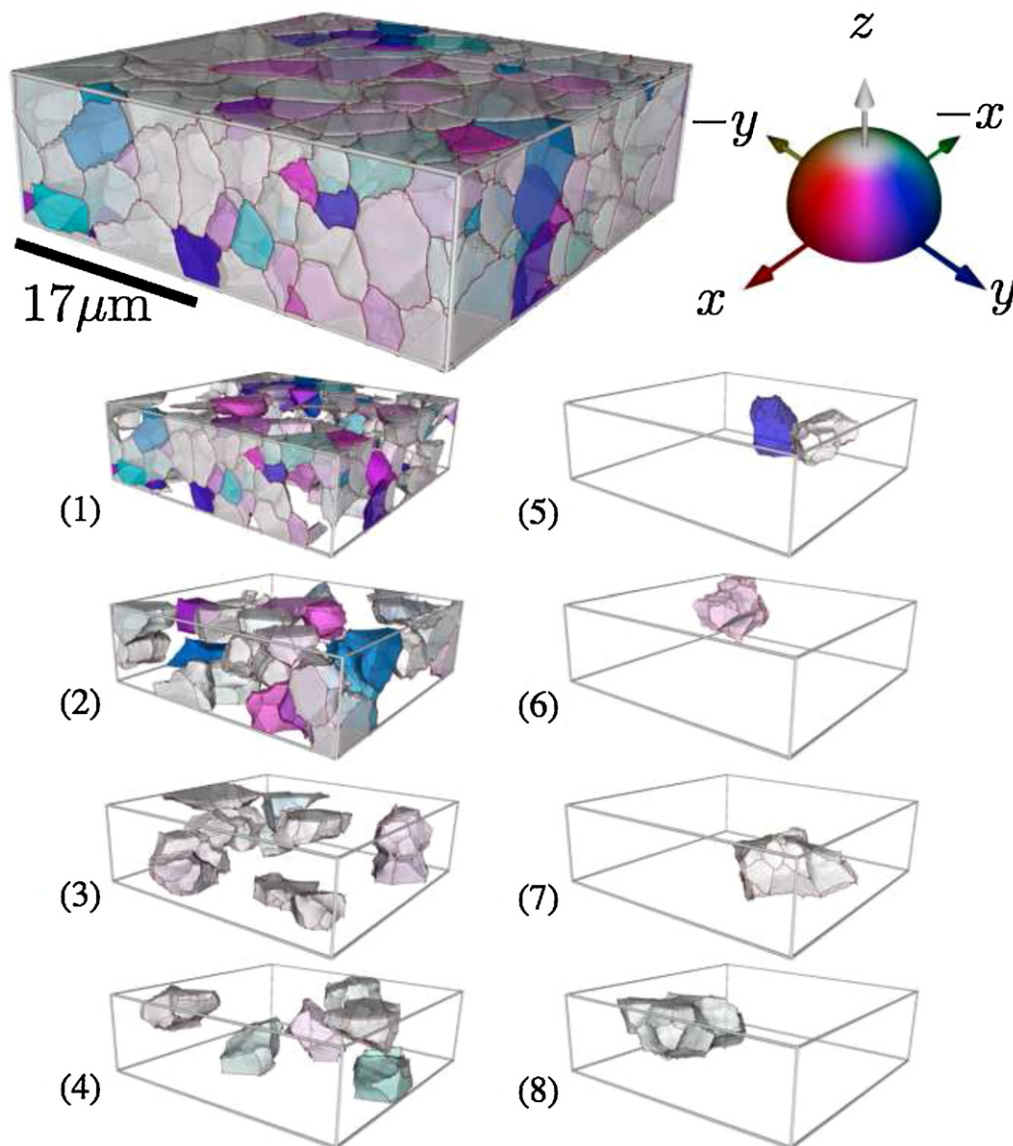
Fig. 3. Three-dimensionally reconstructed, textured, $Bi_{0.5}Na_{0.4}K_{0.1}TiO_3$. Top inset shows overall microstructure. Insets (1)–(8) bin grains into sizes in steps of 12.5% the entire grain size range. The average grain size is 8 μm, the smallest size is 0.45 μm, and the largest grain size is 24 μm. The color of each grain denotes the direction of the pseudocubic a-axis. Just like the untextured sample, medium and large crystals are held together by small grains (see Fig. 2 for comparison). As compared to the untextured sample, insets (3)–(8) show a larger plate-like grain population with a pseudocubic a-axis preferentially aligned with the laboratory reference system z-axis, $i.e.$, the normal to the tape-cast surface during the RTGG processing.

measured. The untextured BNKT sample displayed a piezoelectric response of $d_{33} = 155 \pm 7.8$ pC/N, and the textured sample showed $d_{33} = 227 \pm 11.3$ pC/N, $i.e.$, an improvement of 46% with respect to the untextured sample.

The three-dimensional computer reconstructions of the experimental BNKT samples are shown in Figs. 2, and 3. The measured crystallographic orientation of each volume element of material captures the misorientation correlations that result during processing. Results show that the microstructures are mainly comprised of two grain populations, one large-sized morphologically anisotropic volume fraction of grains, immersed in a smaller grain size population that fills the entirety of the simulation space. In the textured microstructure, Fig. 3, the dispersion of the entire distribution

is broader, and the number of morphologically anisotropic grains is larger, as shown in Fig. 3, insets (2)–(8). The bimodal character of the grain population is a result of using seeds of dimensions and shapes that differ from the starting precursors combined with the grain coarsening that results during sintering.

The simulated macroscopic piezoelectric response of the untextured sample was found to be $d_{33}(MRD = 1) = 163 \pm 10$ pC/N, while for the textured microstructure is $d_{33}(MRD = 4.41) = 217 \pm 15$ pC/N. The agreement between simulated and experimental macroscopic piezoelectric response is within the uncertainty of both samples. In both cases the volume fraction of poled domains was set to $p = 8/10$, in very good agreement with literature values.[28]
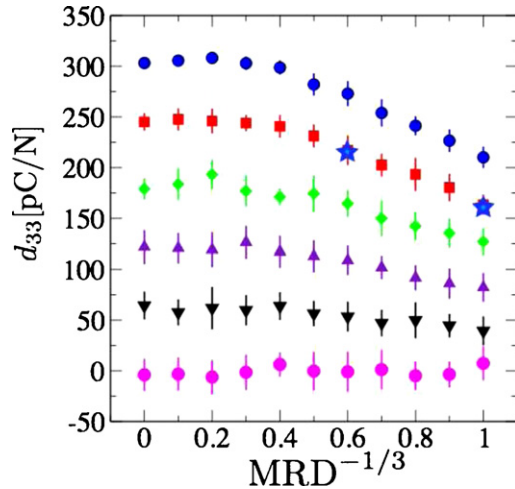
Fig. 4. Effect of crystallographic texture on the macroscopic piezoelectric response for BNKT, d_{33}, as a function of crystallographic texture, $MRD^{-1/3}$, for different amounts of poling, p. ● corresponds to $p = 0$, ▽ to $p = 0.2$, △ to $p = 0.4$, ◇ to $p = 0.6$, □ to $p = 0.8$, and ● to $p = 1$. ★ corresponds to the experimental values as reported herein. Error bars embody the dispersion in response from simulating twenty computer-generated microstructures (see Fig. 5) with the same microstructural parameters.

Fig. 4 summarizes the macroscopic piezoelectric response for BNKT as a function of all accessible and inaccessible crystallographic fiber texture values, MRD, for fixed poling value, MRD_p, by using computer generated microstructures (see Fig. 5). The experimentally determined piezoelectric response for textured and untextured samples is also highlighted. In the limit of perfectly textured samples, i.e., $MRD^{-1/3} = 0$ simulation results agree with measured single-crystal values reported by Izumi et al.[39] and Chiang et al.[12] The results demonstrate that texturing is only beneficial for $MRD_p > 1.5$, i.e., $p > 0.5$, when 50% of the domains not previously aligned in the poling direction have been aligned by the applied electric field. Similarly, the maximum piezoelectric actuation response occurs for $MRD = 125$ and $MRD_p = 2$. Such texture maximizes the sampling of crystallographic orientations closer to the elongational piezoelectric response.

Experimentally, the fabrication of textured samples with poling $p \geq 0.8$ ($MRD_p \geq 1.8$) and $MRD > 8$ ($MRD^{-1/3} < 0.5$) is challenging. However, the analysis shows that no significant macroscopic d_{33} enhancement will result from further increasing the crystallographic texture of the sample beyond what is currently realized through TGG. Nevertheless, simulations also show that a further increase in the material's texture and poling will lead to an increase in mechanical reliability because the degree of misorientation between neighboring grains asymptotically decreases with increasing texture.[62,63]

Simulations demonstrate that the morphological anisotropy of the grains (between 2:1 and 5:1) has no appreciable impact on the macroscopic piezoelectric response. A direct comparison of the different types of grains shown in Fig. 3(1)–(8) against those shown in Fig. 5, insets (1)–(10) demonstrate that the computer generated grains are morphologically isotropic, while those of the reconstructed microstructures are morphologically anisotropic. In both cases,

the macroscopic piezoelectric response is within the uncertainty of the calculation. Therefore, the macroscopic electromechanical response is a function of the volume weighted average contribution to strain along the z-axis of every grain, poling, and the underlying single-crystal properties of each individual domain. As a result, the experimentally textured sample will be 4.41 times more likely with respect to a random sample to find preferentially oriented variants that deliver a piezoelectric response that is closer to alignment to the single-crystal value.

At the microstructural level, the applied average electric field induces local strain variations via the converse piezoelectric effect that yield local stress concentrations, which in turn produce local polarization changes via the direct piezoelectric effect in directions that are not necessarily parallel to the applied electric field (see Figs. 6(a)–(e)). These local changes in polarization induce local electric field deviations that generate an undesired dispersion on the macroscopic properties of the solid and have a direct impact on the long term reliability of the material by focusing electric fields in some grains and shielding it in others. The directions of the induced local electric fields and principal stresses are not necessarily parallel to the macroscopic applied potential difference, but correspond to directions where the electromechanical free energy is minimized, i.e., directions that are mechanically compliant or highly polarizable.[41] The largest variations of stresses, strains, electric fields and gradients of polarization that result from the local electromechanical interactions are found at grain corners, edges, and boundaries. For intermediate stress values, tensile and compressive mechanical fields develop into correlated bicontinous grain networks that are reminiscent of work by Vedula et al.[42] and Fuller et al.[43] Furthermore, the developed stress networks induce the formation of electric field networks via the direct piezoelectric effect (see Fig. 7). The local electromechanical interactions will electrically shield some grains and enhance others. These correlated electrical field and stress networks become sources and sinks of polarization via the converse piezoelectric effect, and are favored locations for ferroelectric fatigue, device depolarization, and domain nucleation and pinning.[44]

At its core, the macroscopic response of polycrystalline piezoelectrics of any chemistry is the result of the local electromechanical interactions and the statistical ensemble of the piezoelectric contribution from individual ferroelectric variants. Specifically, the normalized piezoelectric response of a single tetragonal and rhombohedral variant as a function of orientation is[30]:

$$\frac{\varepsilon_{33}}{(d_{15} + d_{33})E_3} = \frac{d_{33}^L}{d_{15} + d_{33}} = A_{33}\cos^3\alpha + \sin^2\alpha\cos\alpha$$
$$- A_{22}\sin^3\alpha\cos\phi\cos 2\phi \qquad (7)$$

where

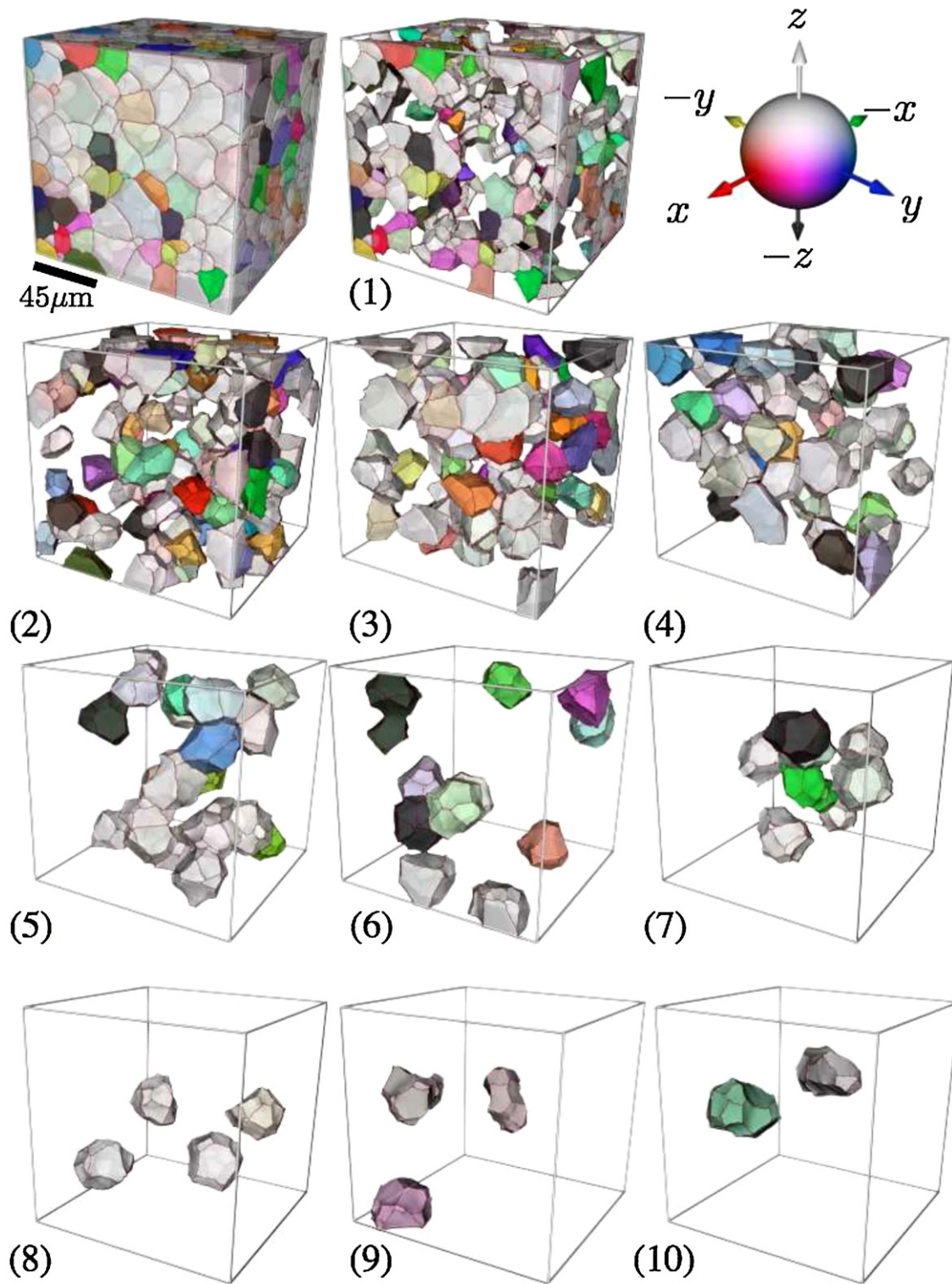$$A_{33} = \frac{d_{33}}{d_{15} + d_{31}} \qquad (8)$$

Fig. 5. Simulated computer-generated polycrystalline microstructure. Insets (1)–(10) allow to visualize the different grain size populations for the simulated microstructure. Average grain size is 2.1 μm, the smallest size is 1 μm, and largest grain size is 3.8 μm. The color of each grain denotes the direction of the *c*-axis. Shown microstructure corresponds to MRD = 1, and *p* = 0. As compared to the reconstructed experimental microstructures, the grains of the computer generated microstructures are morphologically isotropic.

and

$$A_{22} = -\frac{d_{22}}{d_{15} + d_{31}} \tag{9}$$

d_{33}^L is the laboratory reference system longitudinal piezoelectric response for an applied electric field, E_3, along the laboratory *z*-axis. α is the cone-angle that the *c*-axis of the single-crystal makes with the poling axis, and ϕ is the azimuthal angle
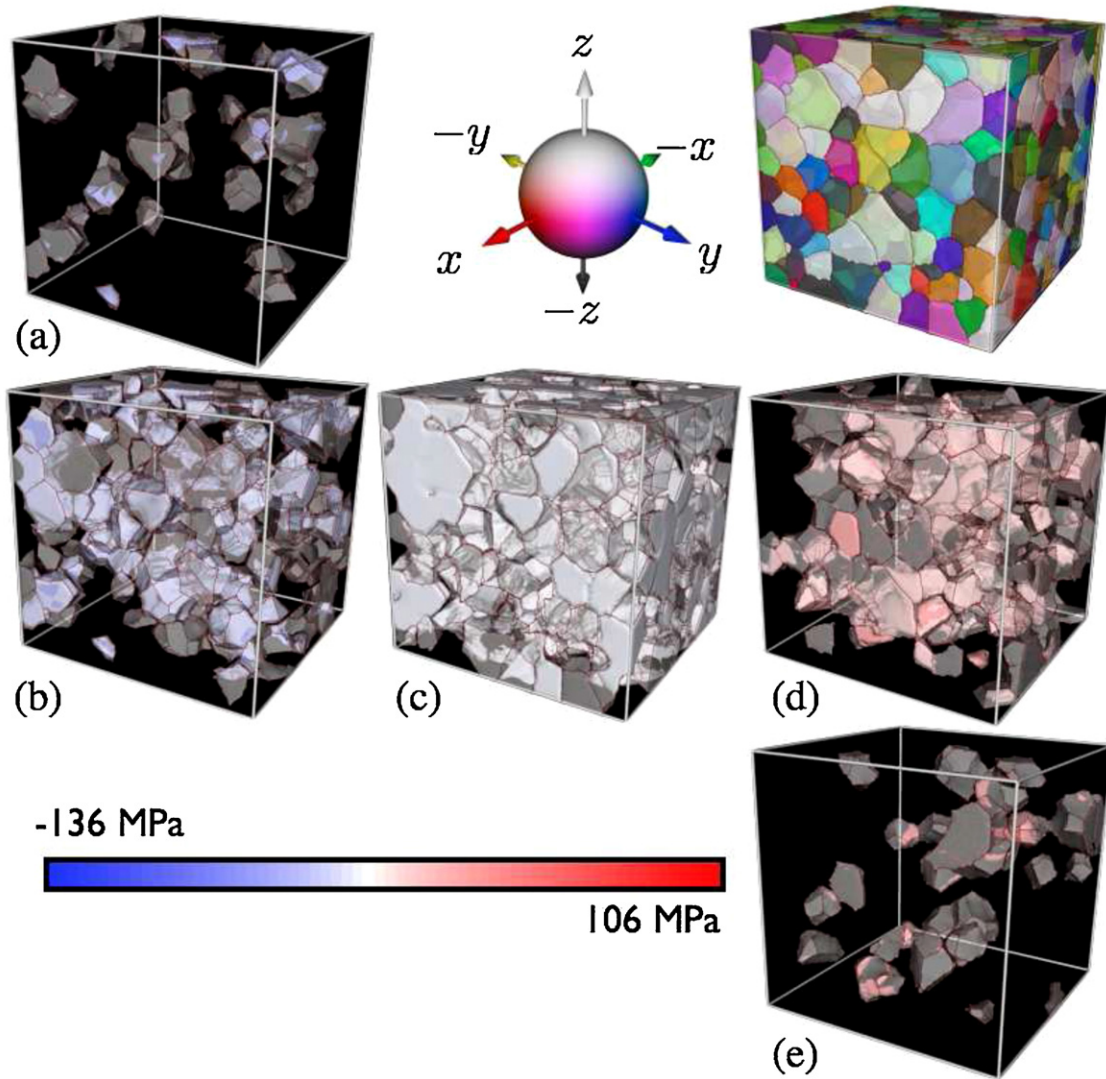
Fig. 6. Hydrostatic stress distribution for a representative microstructure of MRD = 1, $p_F = 0$: (a) corresponds to a compressive stress of $\sigma_h = -136$MPa, (b) to $\sigma_h = -68$MPa, (c) to those locations in the microstructure that are stress-free, $\sigma_h = 0$MPa, (d) to a tensile stress of $\sigma_h = 53$MPa, and (e) to microstructural locations that reach values of $\sigma_h = 106$MPa. Simulations show that stress concentrations occur at grain corners and boundaries, while the macroscopic surfaces of the polycrystal tend to be stress-free.

necessary to bring into alignment the *a*-axis with the laboratory reference system's *x*-axis. A_{33} is defined herein as the normalized tetragonal crystallographic anisotropy, and A_{22} is defined as the normalized rhombohedral crystallographic anisotropy. Thus, for rhombohedral materials ($R3c$) $A_{33}, A_{22} \neq 0$, and for tetragonal materials (4 mm), $A_{22} = 0$.

In this context, the maximal piezoelectric response of a polycrystal is defined by orienting a statistically significant fraction of domains so that its crystallographic orientation maximizes Eq. (7) along the poling axis. Such orientation corresponds to the optimal orientation of the single-crystal, and is shown in Fig. 8 as a function of crystallographic anisotropy, A_{33} and A_{22}. Analytical calculations show that for tetragonal materials, an optimal crystallographic orientation exists if $A_{33} < 2/3$ and $A_{22} \geq 0$. Moreover, in the limit of $A_{33}, A_{22} \to 0$ the optimal crystallographic orientation for all tetragonal and rhombohedral piezoelectric materials converges to $\alpha_c = \arccos[1/\sqrt{3}]$, *i.e.*, close to the {1 1 1} family of planes.

Fig. 8 demonstrates that optimal single-crystal orientations can be sampled by textured polycrystals with small values of normalized anisotropy, $A_{ii} \sim 0$, and weak textures (MRD < 10) because the probability of sampling large angles is more likely to occur in untextured or weakly textured samples. In contrast, materials with small optimal angles, $\alpha \ll \alpha_c$, are defined by large A_{ii} values, and demand large crystallographic textures (MRD ≫ 1) and prohibitively large values of poling in order to observe any texture benefits.

Fig. 9(a)–(c) demonstrate the validity of this assertion. Inset (a) shows that for tetragonal BaTiO$_3$, $A_{33} = 0.24$, $A_{22} = 0$, the optimal texture corresponds to MRD ∼ 1.8, MRD$_p$ = 1 which favors the sampling of $\alpha \sim 49°$, the optimal angle for such chemistry. Fig. 9(c) shows the other extreme of behavior for pseudotetragonal PMN–33% PT, $A_{33} = 2.57$, $A_{22} = 0$. Here, because $A_{33} > 2/3$ no optimal crystallographic orientation away from perfect alignment exists, and thus the optimal response occurs as MRD approaches infinity. Such a texture regime
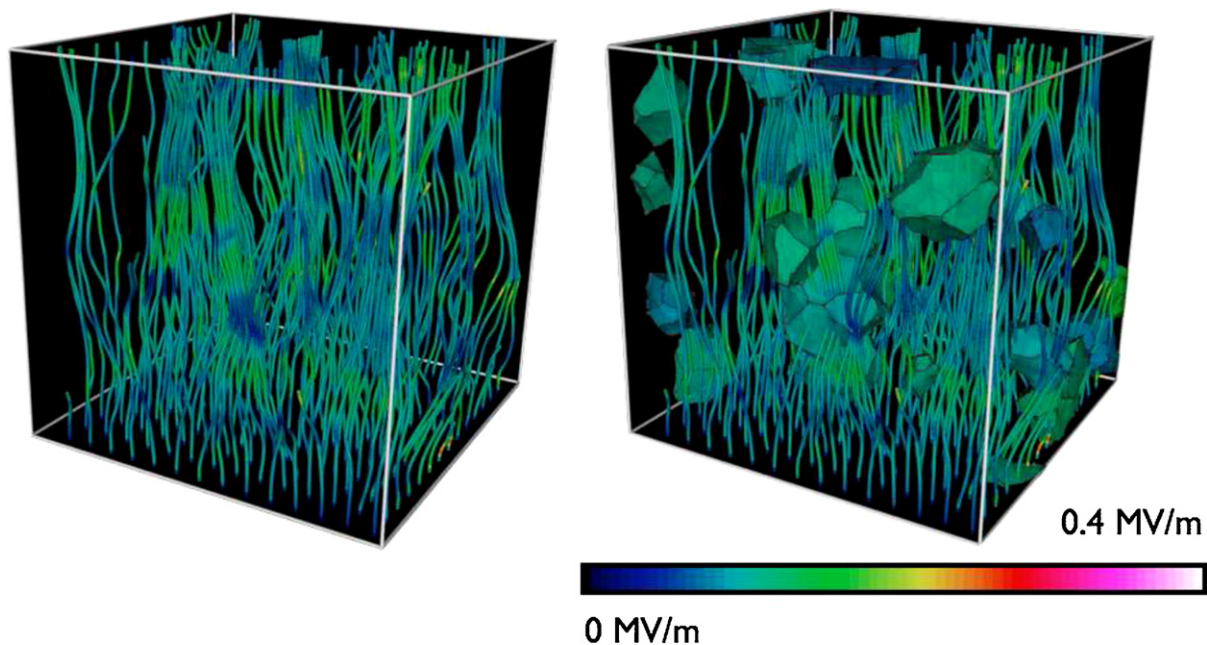
Fig. 7. Top: stream lines of the electric field for a representative microstructure of MRD = 1. Colors correspond to magnitude of electric field. Bottom: representative grains are shown as guide to the eye to illustrate the electric field deflection or concentration as a result of the crystallographic anisotropy and local grain misorientations. Stream lines are uniformly seeded at the bottom face, and interact with grains to form streamline bundles, which are a result of the direct piezoelectric effect, the crystallographic anisotropy, and grain–grain interactions.

is experimentally inaccessible in polycrystals. At the microstructural level, both $BaTiO_3$ and PMN–33% PT sample shear contributions of strain from d_{15} along the poling axis as the crystallographic texture of the polycrystal transitions to complete randomness. Such effect macroscopically produces an apparent d_{33} enhancement for cases where the single-crystal $d_{33} < d_{15}$ (Fig. 9(a)), or is uniformly suppressed for cases where the single-crystal $d_{33} > d_{15}$ (Fig. 9(c)).[65,64]

Finally, Fig. 9(b), shows the macroscopic normalized response of rhombohedral BNKT, i.e., $A_{33} = 0.047$, $A_{22} = 0.33$. For BNKT, the optimal crystallographic orientation corresponds to $\alpha \sim 45°$. For this chemistry, however, such a maximum is not observed because the negative contributions to shear from d_{22} are statistically balanced by positive shear contributions from d_{15}, and lead to the asymptotically decreasing d_{33} behavior. The interplay of contributions of individual piezoelectric coefficients
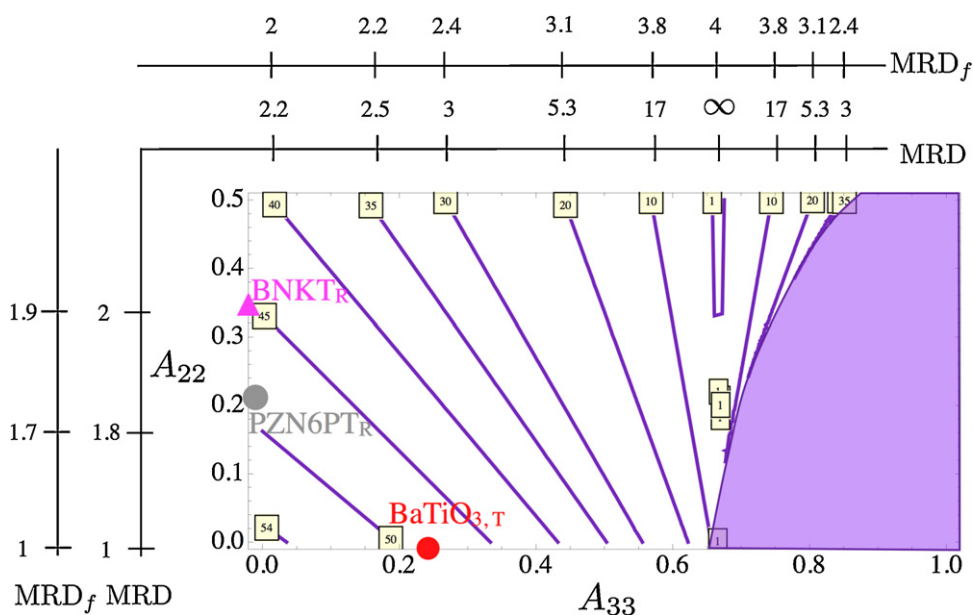

Fig. 8. Isocontour map of optimal crystallographic orientations and associated crystallographic, MRD, and ferroelastic texture, MRD_f. Optimal orientations are found outside the shaded area. A few known chemistries are highlighted, and their macroscopic d_{33} is predicted as a function of fiber texture parameter in Fig. 9.
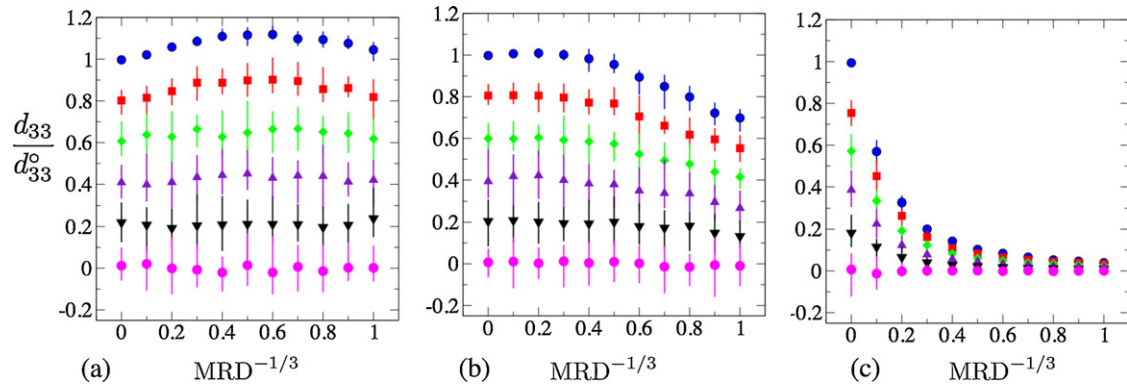
Fig. 9. Effect of texture on the macroscopic d_{33} response for selected anisotropic characteristics: (a) corresponds to $A_{33} = 0.24$; $A_{22} = 0$ (tetragonal Barium Titanate), (b) to $A_{33} = 0.047$; $A_{22} = 0.33$ (rhombohedral BNKT), and (c) $A_{33} = 2.57$; $A_{22} = 0$ (pseudotetragonal PMN–33% PT). In each inset, ● corresponds to $p_F = 0$, ▽ to $p_F = 0.2$, △ to $p_F = 0.4$, ◇ to $p_F = 0.6$, □ to $p_F = 0.8$, and ● to $p_F = 1$. $d_{33}°$ corresponds to the fiber-axis aligned, single-crystal elongational piezoelectric response.

of opposite sign ultimately suppresses the appearance of the optimal piezoelectric response in the limit of weak textures, for shear texture contributions dominate the response of the system. In this context, the exploration of BNKT chemistries with favorable d_{22} values enables the possibility of engineering bulk ceramics with macroscopic responses close or superior to the corresponding single crystal, for the same degree of poling.

Overall, the crystallographic anisotropy–texture map summarized in Fig. 8 provides a simple guideline to establish relationships between single-crystal properties and optimal crystallographic and ferroelastic textures for a fixed A_{33} and A_{22} values, as determined by an individual material chemistry. The proposed description can be readily used as a gauge to discard single-crystal candidates from a portfolio of available chemistries, *e.g.*, by using combinatorial chemistry, *ab initio* calculations,[22–25] or through approaches that make use of the Goldschmidt tolerance factor.[45]

Acknowledgments

Appendix A. Measured and simulated material properties

Tables 1–4.

Appendix B.

Mathematically, texture is quantified by specifying the crystallographic orientation probability distribution, $P_T(\vec{t}, \overset{\leftrightarrow}{g}(\alpha, \beta, \gamma))$, which determines the probability of finding a crystallographic axis between the orientations $\overset{\leftrightarrow}{g}$ and $\overset{\leftrightarrow}{g} + d\overset{\leftrightarrow}{g}$.[55,56] $\vec{t}$ is the vector of fitting texture parameters. α, β, and γ represent an unspecified set of angles that describe the

Table 1
Physical properties of single-crystal rhombohedral $Bi_{0.5}Na_{0.4}K_{0.1}TiO_3$, BNKT. Used properties were adapted from available experimental data.[12,54,11] Missing information was complemented by using numbers from rhombohedral PMN–33% PT,[53] and assuming they both share similar normalized degree of crystallographic anisotropy.

C_{11}	201.2 GPa	d_{33}	303.92 pC/N
C_{33}	171.2 GPa	d_{31}	−143.96 pC/N
C_{44}	29 GPa	d_{22}	2143.45 pC/N
C_{12}	73.6 GPa	d_{15}	6558.31 pC/N
C_{13}	115 GPa	ϵ_{11}	6.437 nF/m
C_{14}	41.5 GPa	ϵ_{33}	6.286 nF/m

Table 2
Physical properties of single-crystal, tetragonal, $BaTiO_3$.[51]

C_{11}	275.1 GPa	d_{33}	85.7 pC/N
C_{33}	164.8 GPa	d_{31}	−34.7 pC/N
C_{44}	54.4 GPa	d_{15}	392 pC/N
C_{12}	178.9 GPa	ϵ_{11}	17.4 nF/m
C_{13}	151.6 GPa	ϵ_{33}	0.96 nF/m

Table 3
Physical properties of single-crystal, pseudotetragonal, PMN–33% PT. Data was compiled from multidomain samples.[52]

C_{11}	115.4 GPa	d_{33}	2820 pC/N
C_{33}	104.6 GPa	d_{31}	−1338 pC/N
C_{44}	69 GPa	d_{15}	146 pC/N
C_{12}	103.4 GPa	ϵ_{11}	14.167 nF/m
C_{13}	102 GPa	ϵ_{33}	73.047 nF/m

Table 4
Experimentally and numerically determined elongational piezoelectric constants for rhombohedral $Bi_{0.5}Na_{0.5-x}K_xTiO_3$, BNKT.

Characteristic	Untextured	Textured
Space group	$R3c$	$R3c$
Crystallographic texture	$L = 0$ (1MRD)	$L = 0.5$ (4.41MRD)
d_{33} (measured)	155±7.8 pC/N	227±11.3 pC/N
d_{33} (predicted)	163±10 pC/N	217±15 pC/N

rotation matrix, $\overleftrightarrow{g}(\alpha, \beta, \gamma)$, to bring the laboratory reference system into alignment with the crystallographic reference system. In particular, crystallographic texture is present in a polycrystalline material if at least one of the crystallographic axes of an individual uniform material phase, *e.g.*, the *c*-axis of a domain, has a greater-than-random probability of alignment with respect to a laboratory reference system direction, *i.e.*, the textured or fiber axis.

$$\mathsf{MRD}_f^{\{111\}} = \frac{4I_{\{111\}}/I^\circ_{\{111\}}}{I_{\{111\}}/I^\circ_{\{111\}} + I_{\{\bar{1}11\}}/I^\circ_{\{\bar{1}11\}} + I_{\{1\bar{1}1\}}/I^\circ_{\{1\bar{1}1\}} + I_{\{11\bar{1}\}}/I^\circ_{\{11\bar{1}\}}} \tag{13}$$

In general, the crystallographic texture displayed by a polycrystalline ferroelectric is a combination of multiple coexisting subpopulations,[32] as specified first during powder processing and sintering, and second during poling. Mathematically, crystallographic texture is described through the expression: $p(\alpha_{\{hkl\}}, \beta_{\{hkl\}}, \gamma_{\{hkl\}}) \sin \alpha_{\{hkl\}} = \sum_{i=1}^{N_T} P_i(\vec{t}_i, \alpha_{\{hkl\}}, \beta_{\{hkl\}}, \gamma_{\{hkl\}})$, where $p(\alpha_{\{hkl\}}, \beta_{\{hkl\}}, \gamma_{\{hkl\}})$ is the volume fraction of material at a crystallographic orientation $(\alpha_{\{hkl\}}, \beta_{\{hkl\}}, \gamma_{\{hkl\}})$, $P_i(\cdot)$ is the orientation probability distribution of the *i*th population, and N_T is the number of discernible subpopulations that can be specified by a linearly independent basis of functions.[57–59] In the limit of a single population, such expression reduces to:

$$p(\alpha_{\{hkl\}}, \beta_{\{hkl\}}, \gamma_{\{hkl\}}) \sin \alpha_{\{hkl\}}$$
$$= P(\vec{t}, \alpha_{\{hkl\}}, \beta_{\{hkl\}}, \gamma_{\{hkl\}}). \tag{10}$$

The probability of finding a volume element of material at a specified crystallographic orientation in a textured sample, with respect to the probability of finding the same orientation in a perfectly untextured sample defines the *crystallographic Multiples of Random Distribution*, MRD,[55,60,33,62] *i.e.*,

$$\mathsf{MRD}(\alpha_{\{hkl\}}, \beta_{\{hkl\}}, \gamma_{\{hkl\}}) = \frac{p(\vec{t}, \alpha_{\{hkl\}}, \beta_{\{hkl\}}, \gamma_{\{hkl\}})}{p(\vec{t}_R, \alpha_{\{hkl\}}, \beta_{\{hkl\}}, \gamma_{\{hkl\}})} \tag{11}$$

where $p(\vec{t}_R, \alpha_{\{hkl\}}, \beta_{\{hkl\}}, \gamma_{\{hkl\}})$ is the volume fraction of material at an orientation $(\alpha_{\{hkl\}}, \beta_{\{hkl\}}, \gamma_{\{hkl\}})$ for an untextured sample, with a texture parameter, $\vec{t} = \vec{t}_R$. A strict probabilistic measure of texture in terms of Multiples of Random Distribution defines the number of times that a differential volume element of material at a defined orientation can be sampled with respect to the number of times it can be sampled in a perfectly untextured sample. Therefore, if a crystallographic orientation is sampled with the same frequency as an untextured sample, MRD = 1. In contrast, if a crystallographic orientation is sampled in a perfectly poled single-crystal, MRD = ∞, and indicates that a crystallographic orientation can always be sampled in an infinitely large polycrystal, and thus will be sampled an infinite number of times more often than in an untextured polycrystal.[55,33]

In turn, *ferroelastic texture*, described in terms of Multiples of Random Distribution, MRD_f,[60] is defined herein as the probability of finding a specific ferroelastic variant, $(\alpha_{V_i}, \beta_{V_i}, \gamma_{V_i})$,

with respect to the probability of finding any of the *N* crystallographically possible variants, *i.e.*,

$$\mathsf{MRD}_f(\alpha_{V_i}, \beta_{V_i}, \gamma_{V_i}) = \frac{N p(\vec{t}, \alpha_{V_i}, \beta_{V_i}, \gamma_{V_i})}{\sum_{j=1}^N p(\vec{t}, \alpha_{V_j}, \beta_{V_j}, \gamma_{V_j})} \tag{12}$$

Eq. (12) is shown to be equivalent to the well-known expression of MRD_f reported by Bowman et al.,[36,61] and used extensively in the literature:

by noting that the measured intensity of diffracted radiation by a polycrystalline solid is proportional to the volume fraction of favorably aligned Bragg planes, $p(\alpha_{\{hkl\}}, \beta_{\{hkl\}}, \gamma_{\{hkl\}})$ [66,55,63]:

$$I(\alpha_{\{hkl\}}, \beta_{\{hkl\}}, \gamma_{\{hkl\}}) = I^\circ_{\{hkl\}} p(\alpha_{\{hkl\}}, \beta_{\{hkl\}}, \gamma_{\{hkl\}}) \tag{14}$$

Here, $I^\circ_{\{hkl\}}$ is the intensity of the $\{hkl\}$ family of crystallographically equivalent diffracting planes of a single-domain, single-crystal at an orientation $(\alpha_{\{hkl\}}, \beta_{\{hkl\}}, \gamma_{\{hkl\}})$. $I^\circ_{\{hkl\}}$ embodies contributions from the experimental setup, such as the Lorentz polarization and monochromator factors, and the structure factor for the diffracting plane.[32,66,55] Direct substitution of Eq. (14) into Eq. (13) leads directly to Eq. (12). Finally, Eq. (4) can be readily derived by directly substituting Eq. (3) into Eq. (12) and simplifying.

The degree of polarization of a volume element of material, p_F, is defined herein as the normalized macroscopic remnant polarization projection of a solid. Thus, $p_F = 0$ for an unpoled single-crystal sample, and as $p_F = 1$ for a perfectly poled sample. Therefore, the number of times a positively polarized axis is counted in a poled, infinitely large solid with respect to the number of times it is counted in an unpoled sample is defined as the *polarization Multiples of Random Distribution*, MRD_p, and is specified through the expression $\mathsf{MRD}_p = 1 + p_F$. Thus, for an unpoled single-crystal, $p_F = 0$, and corresponds to $\mathsf{MRD}_p = 1$, *i.e.*, positively and negatively oriented polarization domains are equally probable. Similarly, for a perfectly poled sample, $p_F = 1$, and corresponds to $\mathsf{MRD}_p = 2$, *i.e.*, every volume element of material is in perfect alignment with the poling axis.

Finally, *ferroelectric texture*, described in terms of Multiples of Random Distribution, MRD_F, corresponds to the number of times a ferroelectric variant can be sampled in a polycrystalline ferroelectric with respect to the number of times a ferroelectric variant can be sampled in an untextured, unpoled ferroelectric solid. MRD_F distinguishes between the antiparallel orientations of each ferroelastic variant, as specified through electrical poling. The probability to sample a polarization axis is proportional to the polarization texture, MRD_p, and is thus defined as shown in Eq. (5).

References

1. Rödel J, Jo W, Seifert KTP, Anton E-M, Granzow T. Perspective on the development of lead-free piezoceramics. *J Am Ceram Soc* 2009;**92**:1153–77.
2. Zhang S, Xia R, Shrout TR. Lead-free piezoelectric ceramics vs. PZT. *J Electroceram* 2007;**19**:251–7.

3. Liu W, Ren X. Large piezoelectric effect in Pb-free ceramics. *PRL* 2009;**103**:257602.

4. Saito Y, Takao H, Tani T, Nonoyama T, Takatori K, Homma T, et al. Lead-free piezoceramics. *Nature* 2004;**432**:84–7.

5. Xu S, Qin Y, Xu C, Wei Y, Yang R, Wang ZL. Self-powered nanowire devices. *Nat Nanotechnol* 2010;**5**:366–73.

6. Messing GL, Troilier-McKinstry S, Sabolsky EM, Duran C, Kwon S, Brahmaroutu B, et al. Templated grain growth of textured piezoelectric ceramics. *Solid State Mater Sci* 2004;**28**:45–96.

7. Tani T. Crystalline-oriented piezoelectric bulk ceramics with perovskite-type structure. *J Korean Phys Soc* 1998;**32**:1217–20.

8. Saito Y, Takao H. Synthesis of plate-like $(Bi_{0.5}Na_{0.5})TiO_3$ particles by using topochemical microcrystal conversion method and grain-oriented ceramics. *J Korean Phys Soc* 2007;**51**:790–7.

9. Gao F, Liu X-C, Zhang C-S, Cheng L-H, Tian CS. Fabrication and electrical properties of textured $(Na, K)_{0.5}Bi_{0.5}TiO_3$ ceramics by reactive-templated grain growth. *Ceram Int* 2008;**34**:403–8.

10. Tani T. Texture engineering of electronic ceramics by the reactive-templated grain growth method. *J Ceram Soc Jpn* 2006;**114**:363–70.

11. Yi X, Chen H, Cao W, Zhao M, Yang D, Ma G, et al. Flux growth and characterization of lead-free piezoelectric single crystal $Bi_{0.5}(Na_{1-x}K_x)_{0.5}TiO_3$. *J Cryst Growth* 2005;**281**:364–9.

12. Chiang Y-M, Farrey GW, Soukhojak AN. Lead-free high-strain single-crystal piezoelectrics in the alkaline–bismuth–titanate perovskite family. *Appl Phys Lett* 1998;**25**:3683–5.

13. Rayleigh JWS. On the influence of obstacles arranged in rectangular order upon the properties of the medium. *Philos Mag* 1892;**34**:481–502.

14. Eshelby JD. The determination of the field of an ellipsoidal inclusion and related problems. *Proc Roy Soc Lond A* 1957;**241**:37696.

15. Deeg WFJ. The analysis of dislocation, crack, and inclusion problems in piezoelectric solids. PhD thesis. Department of Materials Science and Engineering. Stanford University; 1980.

16. Pertsev NA. Aggregate linear properties of ferroelectric ceramics and polycrystalline thin films: calculation by the method of effective piezoelectric medium. *J Appl Phys* 1995;**84**:1524–9.

17. Zembil'gotov AG, Pertsev NA, Wazer R. Effective dielectric and piezoelectric constants of thin polycrystalline ferroelectric films. *Phys Solid State* 1998;**40**:2002–8.

18. McMeeking RE, Hwang S, Huber JE, Fleck NA. The simulation of switching in polycrystalline ferroelectric ceramics. *J Appl Phys* 1998;**84**:1530–40.

19. Olson T, Avellaneda M. Effective dielectric and elastic constants of piezoelectric polycrystals. *J Appl Phys* 1992;**71**:4455–64.

20. Aleshin V. Properties of anisotropic piezoactive polycrystals. *J Appl Phys* 2000;**88**:3587–91.

21. Li JY. The effective electroelastic moduli of textured piezoelectric polycrystalline aggregates. *J Mech Phys Solids* 2000;**48**:529–52.

22. Wahl R, Vogtenhuber D, Kresse G. $SrTiO_3$ and $BaTiO_3$ revisited using the projector augmented wave method: performance of hybrid and semilocal functionals. *Phys Rev B* 2008;**78**:104–16.

23. Wu X, Vanderbilt D, Hamann DR. Systematic treatment of displacements, strains, and electric fields in density functional perturbation theory. *Phys Rev B* 2005;**72**:035105.

24. Zhing W, Vanderbilt D, Rabe KM. Phase transitions in $BaTiO_3$ from first principles. *Phys Rev Lett* 1994;**73**:1861–4.

25. Meyer B, Vanderbilt D. Ab initio study of ferroelectric domain walls in $PbTiO_3$. *Phys Rev B* 2002;**65**:104111.

26. Zhang W, Bhattacharya K. A computation model of ferroelectric domains. Part I. Model formulation and domain switching and Part II. Grain boundaries and defect pinning. *Acta Mater* 2005;**53**:185–209.

27. Hu HL, Chen L-Q. Three-dimensional computer simulation of ferroelectric domain formation. *J Am Ceram Soc* 1998;**81**:492–500.

28. Li JY, Rogan RC, Ustundag E, Bhattacharya K. Domain switching in polycrystalline ferroelectric ceramics. *Nat Mater* 2005;**4**:776–81.

29. Zhang JX, Wu R, Choudhury S, Li YL, Hu SY, Chen L-Q. Three-dimensional phase-field simulation of domain structures in ferroelectric islands. *Appl Phys Lett* 2008;**92**:122906.

30. Nye JF. *Physical properties of crystals. Their representations by tensors and matrices*. 2nd ed. New York: Oxford University Press; 1985.

31. Anderson MP, Crest GS, Srolovitz DJ. Computer simulation of normal grain growth in three dimensions. *Philos Mag* 1989;**B59**:293–329.

32. Dollase WA. Correction of intensities for preferred orientation in powder diffractometry: application of the March model. *J Appl Crystallogr* 1986;**19**:267–72.

33. Blendell JE, Vaudin MD, Fuller Jr ER. Determination of texture from individual grain orientation measurements. *J Am Ceram Soc* 1999;**82**: 3217–20.

34. Seabaugh MM, Vaudin MD, Cline JP, Messing GL. Comparison of texture analysis techniques for highly oriented a-Al_2O_3. *J Am Ceram Soc* 2000;**83**:2049–54.

35. Lotgering FK. Topotactical reactions with ferrimagnetic oxides having hexagonal crystal structures-I. *J Inorg Nuclear Chem* 1959;**9**:113–23.

36. Jones J, Iverson B, Bowman K. Texture and anisotropy of polycrystalline piezoelectrics. *J Am Ceram Soc* 2007;**90**:2297–314.

37. Jones JL, Hoffman M, Bowman KJ. Saturated domain switching textures and strains in ferroelastic ceramics. *J Appl Phys* 2005;**98**:024115.

38. Key T, García RE, Vaudin MD, Bowman KJ, Tani T, Jo W, et al. A method to correlate crystallographic, ferroelastic, ferroelectric, and lotgering texture in lead-free ferroelectric ceramics. In preparation.

39. Izumi M, Yamamoto K, Suzuki M, Noguchi Y, Miyayama M. Large electric field-induced strain in $Bi_{0.5}Na_{0.5}TiO_3$–$Bi_{0.5}K_{0.5}TiO_3$ solid solution single crystals. *APL* 2008;**93**:242903.

40. Jones GO, Thomas PA. Investigation of the structure and phase transitions in the novel A-site substituted distorted perovskite compound $Na_{0.5}Bi_{0.5}TiO_3$. *Acta Cryst* 2002;**B58**:168–78.

41. García RE, Bishop CM, Carter WC. Thermodynamically consistent variational principles with applications to electrically and magnetically active systems. *Acta Mater* 2004;**52**:11–21.

42. Vedula VR, Glass SJ, Saylor DM, Rohrer GS, Carter WC, Langer SA. Residual stress predictions in polycrystalline alumina. *J Am Ceram Soc* 2001;**84**:2947–54.

43. Saylor DM, Fuller Jr ER, Weiss T. Thermal-elastic response of marble polycrystals: influence of grain orientation configuration. *Int J Mater Res* 2007;**98**:1256–63.

44. Zhukov S, Genenko YA, Hirsch O, Glaum J, Granzow T. Dynamics of polarization reversal in virgin and fatigued ferroelectric ceramics by inhomogeneous field mechanism. *Phys Rev B* 2010;**82**:014109.

45. Goldschmidt VM, Oslo I. Geochemical distribution laws of the elements. VII. The laws of crystal chemistry. *Mater Nat* 1926;**2**:7–12.

46. APC International, Ltd. http://www.americanpiezo.com/

47. Erhart J, Burianova L. What is really measured on a d33-meter? *J Eur Ceram Soc* 2001;**21**:1412–5.

48. Lutterotti L, Matthies S, Wenk H-R. MAUD (material analysis using diffraction): a user friendly Java program for Rietveld texture analysis and more. In: *Proceeding of the 12th International Conference on Textures of Materials (ICOTOM-12), vol. 1*. 1999. p. 1599.

49. Jones GO, Kreisel J, Thomas PA. A structural study of the $(Na_{1-x}K_x)0.5$ $Bi_{0.5}TiO_3$ perovskite series as a function of substitution (x) and temperature. *Powder Diffraction* 2002;**17**:301–19.

50. Li J, Dillon SJ, Rohrer GS. *Acta Mater* 2009;**57**:4304–11.

51. Jona F, Shirane G. *Ferroelectric crystals*. NY, USA: Dover Publications Inc.; 1993.

52. Yin J, Jiang B, Cao W. Elastic, piezoelectric, and dielectric properties of 0.955 $Pb(Zn_{1/3}Nb_{2/3})O_3$–0.45 $PbTiO_3$ single crystal with designed multidomains. *IEEE Trans Ultrasonics Ferroelectrics Frequency Control* 2000;**47**:285–91.

53. Zhang R, Jiang B, Cao W. Single-domain properties of 0.67 $Pb(Mg_{1/3}Nb_{2/3})O_3$–0.33 $PbTiO_3$ single crystals under electric field bias. *Appl Phys Lett* 2003;**82**:787–9.

54. Luo H. Personal communication; April, 2010.

55. Bunge H-J. *Texture analysis in materials science*. 1st ed. London: Butterworths; 1993.

56. Moraweic A. *Orientations and rotations: computations in crystallographic textures*. 1st ed. Germany: Springer Publishing Company; 2004.

57. Frary M, Schuh CA. Grain boundary networks: scaling laws, preferred cluster structure, and their implications for grain boundary engineering. *Acta Mater* 2005;**53**:4323–35.

58. Schuh CA, Minich RW, Kumar M. Connectivity and percolation in simulated grain boundary networks. *Philos Mag* 2003;**A83**:711–26.

59. Minich RW, Schuh CA, Kumar M. The role of topological constraints on the statistical properties of grain boundary networks. *Phys Rev B* 2002;**66**:052101.

60. Jones J, Slamovich EB, Bowman KJ. Domain texture distributions in tetragonal lead zirconate titanate by X-ray and neutron diffraction. *J Appl Phys* 2005;**97**:034113.

61. Jones JL, Slamovich EB, Bowman KJ. Critical evaluation of the.lotgering degree of orientation texture indicator. *J Mater Res* 2004;**19**:3414–22.

62. Rohrer GS, Saylor DM, Dasher BE, Adams BL, Rollet AD, Wynblatt Ltdc P. The distribution of internal interfaces in polycrystals. *Int J Mater Res Adv Tech B (basic)* 2004;**95**:1–18.

63. García RE, Vaudin M. Correlations between the crystallographic texture and grain boundary character in polycrystalline materials. *Acta Mater* 2007;**55**:5728–35.

64. García RE, Carter WC, Langer SA. The effect of texture on the macroscopic properties of polycrystalline ferroelectrics. Part 2. Applications to barium titanate and PZN–PT. *J Am Ceram Soc* 2003;**88**:750–7.

65. Davis M, Budimir M, Damjanovic D, Setter N. Rotator and extender ferroelectrics: importance of the shear coefficient to the piezoelectric properties of domain-engineered crystals and ceramics. *J Appl Phys* 2007;**101**:054112.

66. Cullity BD. *Elements of X-ray diffraction*. 2nd ed. Massachusetts: Addison-Wesley Publishing Company; 1978.